CRYSTAL GROWTH & DESIGN

pubs.acs.org/crystal

Article

Direct Visualization of CH_4/CO_2 Hydrate Phase Transitions in Sandstone Pores

Jyoti Shanker Pandey, Ørjan Strand, Nicolas von Solms, Geir Ersland, and Stian Almenningen*

Cite This: *Cryst. Growth Des.* 2021, 21, 2793−2806

Read Online

ACCESS | Metrics & More | Article Recommendations

ABSTRACT: This paper reports the formation and dissociation pattern of hydrate crystals with varying compositions of CH_4 and CO_2 in porous media. Direct visualization was carried out using a high-pressure, water-wet, silicon wafer-based micromodel with a pore network resembling sandstone rock. Hydrate crystals were formed under reservoir conditions (P = 45−65 bar and T = 1.7−3.5 °C) from either a two-phase system consisting of liquid water and a CH_4−CO_2 gas mixture or a three-phase system consisting of liquid water, CH_4-rich gas, and CO_2-rich liquid. A stepwise pressure reduction method was later applied to visualize multiple dissociation events occurring between the equilibrium pressures of pure CH_4 hydrates and pure CO_2 hydrates. The results showed that liberated gas from the initial dissociation became trapped and immobilized by surrounding undissociated hydrate crystals when the initial hydrate saturation was high. Mixing of liberated gas with liquid water led to rapid reformation of hydrates during the stepwise pressure reduction; the reformed hydrate crystals dissociated at a lower pressure close to the equilibrium pressure of pure CO_2 hydrates. The results demonstrate the possibility of producing gas liberated from local hydrate dissociation while simultaneously reforming hydrates in other parts of the sediments. This is relevant for the proposed production method where CO_2 injection in CH_4 hydrate reservoirs is followed by pressure depletion to enhance the CH_4 gas recovery.

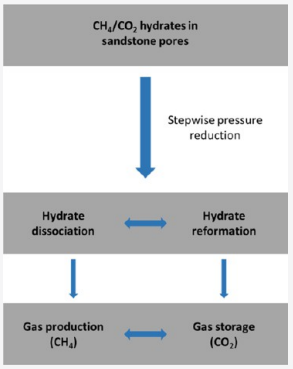

1. INTRODUCTION

Gas hydrates are ice-like crystalline substances formed when guest molecules, such as methane (CH_4) or carbon dioxide (CO_2), react with water at moderate-to-high pressures and low temperatures. Natural gas hydrate reservoirs found in permafrost-affected sediments and in offshore deep-sea sediments are potential targets for CO_2 storage and associated carbon-neutral CH_4 gas production. When CO_2-rich gas is injected into CH_4 hydrate reservoirs, spontaneous CH_4/CO_2 exchange takes place due to differences in the chemical potentials between CH_4 and CO_2 hydrates.[1] The exchange process is driven by favorable thermodynamics and is believed to be characterized by two stages: a rapid surface reaction with partial dissociation followed by solid diffusion of guest molecules penetrating through the formed mixed hydrate layer and deeper into the hydrate crystal.[2,3] A constant rate transformation process in which CH_4 hydrate crystals exposed to CO_2 decreased in size and some even disappeared over time has also been observed.[4] Nevertheless, a collection of mixed hydrates with compositions ranging between pure CH_4 hydrates and pure CO_2 hydrates will form in the reservoir during the CO_2 injection. Heat release will also occur as CO_2 reacts with pore water to form CO_2 hydrates, which may induce dissociation of nearby preexisting CH_4 hydrates. Overall, there will be numerous phase transitions taking place involving mixed hydrates of CH_4 and CO_2. Fundamental knowledge of these phase transitions is essential to enable an accurate modeling of CO_2 injection into CH_4 hydrate reservoirs and to increase the understanding of the CH_4/CO_2 exchange process.

Micromodels have recently been used in experiments to study and visualize gas hydrate pore distributions during formation and dissociation. Tohidi et al.[5] used glass micromodels to visualize CH_4 hydrate formation in the presence of water-soluble tetrahydrofuran at an atmospheric pressure and CH_4 and CO_2 hydrate formation at a high pressure. Katsuki et al.[6] used glass micromodels to study the subcooling effect on CH_4 hydrate growth kinetics. Hauge et al.[7] discussed the formation of pure CH_4 and pure CO_2 hydrates using high-pressure silicon micromodels and concluded that the growth pattern depended on the fluid connectivity and the local fluid distribution. The same micromodels were used by Almenningen et al.[8] to visually determine the phase stability of CH_4 hydrates in sandstone pores. A comprehensive description of the pore-scale growth pattern of CH_4 hydrates was given by Almenningen et al.,[9]

Received: December 21, 2020
Revised: March 19, 2021
Published: April 6, 2021

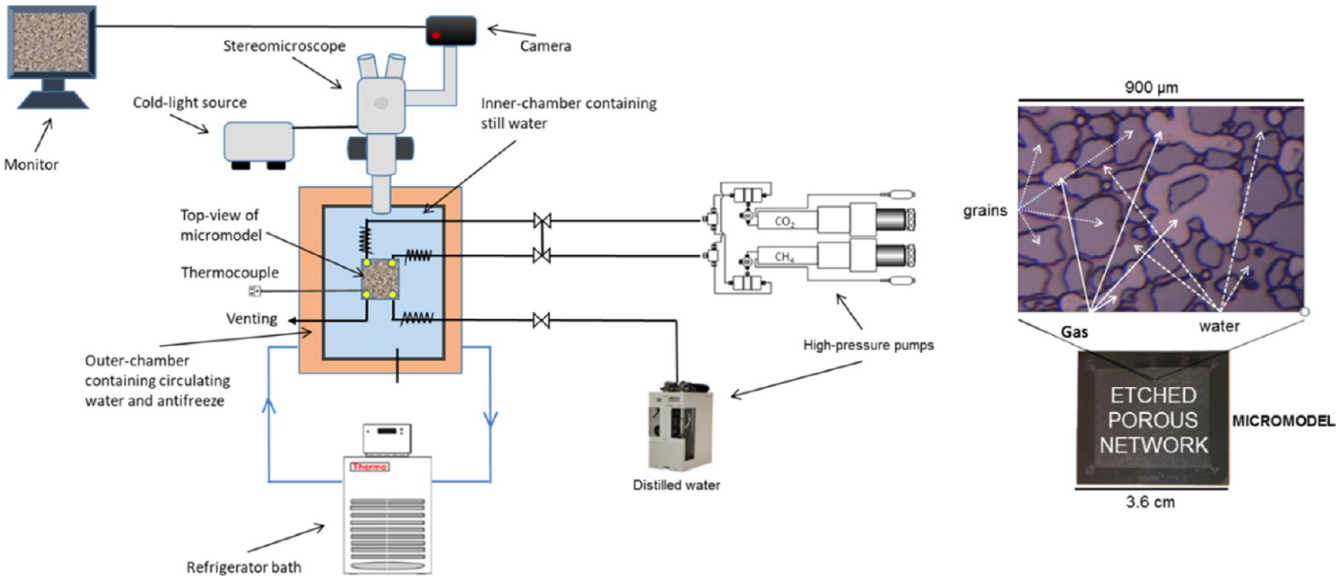

Figure 1. Overview of experimental setup (left) and close-up of the micromodel saturated by gas and water (right). The experimental setup includes high-pressure pumps for injection and production of fluids, a refrigerator bath for controlling the temperature, a microscope, and a camera for recording images of the pore space.

and the nature of CO_2 hydrate self-sealing during CO_2 storage in aquifers was also studied using the micromodels.[10,11]

This paper extends the research on visualization of pore-scale hydrate phase transitions in sediments to include mixtures of CH_4 and CO_2 hydrates. Previous studies on mixed hydrates include equilibria measurements[12,13] and measurements of kinetics and long-term storage potential,[14] but these studies were limited to bulk hydrate investigations using cell reactors. Cell reactors and gas chromatography have also been used to analyze dissociation enthalpies and exchange efficiencies of mixed hydrates in porous media.[15,16] Here, we provide a qualitative analysis of CH_4/CO_2 hydrate formation and subsequent dissociation at a constant temperature above 0 °C using a high-pressure micromodel replicating a cross section of porous sandstone rock. Hydrates were formed at a constant pressure and gradual dissociation was conducted by stepwise depressurization. Direct optical visualization at the pore scale was used to evaluate the effect of fluid phases, saturation, and distribution on hydrate phase transitions in coarse-grained sediments.

2. MATERIALS AND METHODS

2.1. Experimental Setup. The 2D micromodel used in this study was capable of withstanding a pressure up to 150 bar and a temperature down to −3 °C. The model was made of a silicon wafer connected anodically to a borosilicate glass plate on top. A 2D pore network replicating a thin section of Berea sandstone was etched into the silicon wafer with the deep reactive ionic etching (DRIE) technique.[17] The average pore diameter was approximately 100 μm and the pore height was constant and equal to 25 μm. The DRIE technique provided sharp pore corners, rough pore walls, and a high aspect ratio, and the anodic-bonding technique resulted in uniformly water-wetted grains.[8] The solid grains were thus coated with thin water films, while the gas resided in the middle of the pores. The total pore volume of the micromodel was approximately 10 μL.

The micromodel was equipped with a nano-port in each corner of the model (Figure 1). The nano-ports had nano-tubing guides with rubber packing (Upchurch/IDEX), which were connected to high-pressure pumps (Chandler Engineering, Quizix Q5200) using a combination of 1/16″ PEEK (polyetheretherketone) and stainless-steel tubing. Three separate pumps, each filled with either distilled water, CH_4 gas, or liquid CO_2, were connected to separate ports in the micromodel and were used to inject and produce fluids. The pressure sensors in the pumps provided pressure readings of the pore pressure. The micromodel was mounted between two aluminum frames and placed inside the inner chamber of a dual-chamber cooling system. The micromodel was fully submerged in still water in the inner chamber ,while a mixture of antifreeze and water was circulated in the outer chamber using a cooling bath. The outer and inner chambers were separated by aluminum walls, which allowed for a rapid heat exchange between the micromodel and the cooling fluid. The system temperature was measured by a thermocouple (HH506RA Omega Multi-logger) placed in the still water directly beneath the micromodel. The thermal conductivity of the silicon wafer was around 1.3 W/(cm °C) compared to that of water, which is around 0.006 W/(cm °C). The constant temperature of the still water was therefore effectively transferred to the entire micromodel and the temperature gradient within the micromodel was believed to be small. A stereomicroscope (Nikon SMZ1500) connected to a DSLR camera (NikonD7100) were used to visualize and record phase transitions in the pore space. The working distance between the micromodel and the microscope was 54 mm and the field of view (FOV) was of the order of 2 × 2 mm using a 1× objective lens and 110× magnification. A cold-light source (Photonic LED F1, 5500K) was used to illuminate the FOV.

2.2. Experimental Procedure and Data Processing. The micromodel was initially flushed with distilled water to displace the air from the pore space and to ensure 100% water saturation. The pore pressure was then increased to a constant value of 45−65 bar by water injection. The water pump was set to a constant pressure operation, while CH_4 gas was injected into the model from a separate injection port. The pores were then saturated with a given amount of CH_4 gas by water displacement. Afterward, as the CH_4 gas injection was stopped, liquid CO_2 was injected into the model from a separate injection port. The pores were then saturated with a given amount of liquid CO_2 by water and CH_4 gas displacement. The final saturation of water, CH_4 gas, and liquid CO_2 varied between each experiment. The water pump was then shut off and disconnected from the model. The CO_2 pump was also shut off but remained connected to the model, providing a reservoir of liquid CO_2. The CH_4 pump was set to a constant pressure operation and maintained a constant pore pressure during the hydrate formation process, likely resulting in a mixture of hydrates with varying CH_4 and CO_2 compositions. The

https://doi.org/10.1021/acs.cgd.0c01714
Cryst. Growth Des. 2021, 21, 2793−2806

hydrate formation was initiated by reducing the system temperature to a constant value of 1.7−3.5 °C. Hydrates usually started forming 1−2 h after the system temperature was set below the equilibrium temperature of pure CH_4 hydrates. In a few cases, when hydrate nucleation did not start within 5 h, the hydrate formation had to be triggered by flowing CH_4 gas through the pore space for a couple of seconds. The agitation involved with the temporary fluid flow induced hydrate nucleation within minutes after the injection was stopped.

The hydrate formation was terminated after 24 h when the phase transitions stopped and the fluid and hydrate saturations became constant. The CO_2 pump was then disconnected from the micromodel and the pressure was lowered by the CH_4 pump through constant volumetric gas production (10 mL/h) until the pressure reached 1−2 bar above the equilibrium pressure of pure CH_4 hydrates. Hydrate dissociation was initiated by stepwise pressure reductions by the CH_4 pump in decrements of 1 bar. The pressure was kept constant for at least 30 min after each pressure step to allow phase transitions to occur. The stepwise pressure depletion was continued until all solid hydrates dissociated in the FOV.

All phase transitions and changes in saturation were recorded continuously during hydrate growth and dissociation. Pore-scale images were processed and segmented by the software Paint.net. Segmentation of phases allowed for calculation of 2D fluid saturations using a MATLAB code. For instance, the hydrate saturation was calculated by counting the number of pixels attributed to the hydrate phase and dividing that number by the number of pixels attributed to the entire pore space. However, the pores were not strictly 2D because of their vertical depth of 25 μm. Different fluid phases could therefore reside on top of each other in the same pore through the vertical profile, especially when layered hydrates formed at the gas−water interface.[9] Differentiation between hydrate morphologies was then conducted based on the refractive index of each phase (Table 1). The difference in the refractive indices between solid hydrates and gas was used to infer formation of hydrate films along the gas−water interface.[18]

Table 1. Refractive Indices of the Different Fluid Phases

fluid phase	refractive index
gas hydrates	1.35[19]
gas	1.00
liquid water	1.33
liquid CO_2	1.20−1.25[20]

3. RESULTS AND DISCUSSION

3.1. Two-Component Hydrate Phase Transitions: CO_2 and Water. Pure CO_2 hydrate formation was carried out at constant P = 67 bar and T = 3.5 °C (P_{eq} = 18.3 bar) and the hydrate formation sequence is shown in Figure 2. Images 2a (raw) and image 2b (segmented) display the initial fluid distribution of liquid CO_2 (yellow) and liquid water (blue). The initial CO_2 hydrate formation at the CO_2−water interface was quick and the CO_2 hydrate encapsulated the liquid CO_2 within seconds (Figure 2c). The formed CO_2 hydrate film was initially thin, and the hydrate film collapsed and reformed continuously, enabling the liquid CO_2 to displace liquid water in some of the pores (Figure 2d). Uchida et al.[21] observed the propagation of a secondary hydrate film on the CO_2−water interface of a single water droplet within seconds after hydrate nucleation. After several minutes (Figure 2e), the hydrate film reached a thickness that inhibited further movement of the fluid phases. The hydrate film continued to grow slowly during the next 16 h (Figure 2f), but neither was crystallization of hydrates observed in the water phase nor was the CO_2 phase fully consumed by hydrate formation in this experiment. Previous CH_4 and CO_2 hydrate formation and dissociation studies using micromodels suggest that CO_2 hydrates form more easily in the water phase compared to CH_4 hydrates because of the higher CO_2 solubility in water.[7] During CO_2 hydrate formation in a flow experiment, nucleation started at the CO_2−water interface with encapsulation of the liquid CO_2 phase followed by complete crystallization of the liquid water phase.[10] The flow experiment was conducted at a similar pressure as in this study, but the system temperature was 1.3 °C as opposed to 3.5 °C here. This suggests that the likelihood of hydrate crystallization in the water phase increases with increasing driving forces, which was also observed for CH_4 hydrates in another study.[22] The driving forces also control the shape of the hydrate crystals and the hydrate crystal growth rate on the gas−water interface.[23−27] The hydrate nucleation rate is shown to depend on the degree of supersaturation of CH_4 and CO_2 in the liquid water.[28]

The pressure was depleted at a constant volumetric rate equal to 10 mL/h to initiate hydrate dissociation (Figure 3). The first 20 bars of pressure reduction did not change the hydrate saturation or the hydrate morphology as the pressure was still above the equilibrium pressure (Figure 3c). However, the hydrate-encapsulated liquid CO_2 vaporized to gaseous CO_2 as the pressure was lowered below 47 bar. The bubble point pressure for CO_2 in the pump (T = 21 °C) was 58.6 bar, whereas it was 38.2 bar at the system temperature of 3.5 °C.[29] The phase transition led to a darkening of the hydrate film (Figure 3c,d) caused by the decrease of the refractive index of CO_2 as CO_2 converted from liquid to gas. The phase transition of CO_2 in the FOV demonstrated that the pressure depletion was effectuated throughout the pore space and the CO_2 hydrate started to dissociate immediately following pressure depletion below the equilibrium pressure (Figure 3e). The CO_2 hydrate film dissociated predominantly from the center of pores and outward toward the grain walls. The liberated CO_2 gas from the hydrate film escaped the dissociation front through convective flow in the already connected CO_2 gas phase. However, the viscous two-phase flow of water and CO_2, coupled with local temperature depressions because of endothermic hydrate dissociation, led to temporary hydrate reformation in the entire FOV (Figure 3g,h). The hydrate reformation was instant and obstructed the fluid flow in the FOV completely for 4 min. Similar hydrate reformations were observed on a larger scale during depressurization of xenon hydrates.[30]

3.2. Three-Component Hydrate Phase Transitions: CH_4, CO_2, and Water. *3.2.1. Formation of Hydrates with Varying Compositions.* Hydrate formation from CH_4, CO_2, and water was conducted at a constant pressure and temperature for different initial fluid saturations (Table 2). Two experiments (Exp. 2 and 3) had low initial water saturations (S_w < 0.50) and high CH_4-rich gas saturations (S_g > 0.50). Another two experiments (Exp. 4 and 5) had high initial water saturations (S_w > 0.50) and low CH_4 and CO_2 saturations; Exp. 5 had a CH_4-rich gas saturation of 0.34, while Exp. 4 had both a CO_2-rich liquid saturation of 0.30 and a CH_4-rich gas saturation of 0.05. The last experiment (Exp. 6) had close to 100% water saturation with trace amounts of both CH_4-rich gas and CO_2-rich liquid. The pressure and temperature were well within the hydrate stability zone for both pure CO_2 hydrates and pure CH_4 hydrates (Figure 4).

https://doi.org/10.1021/acs.cgd.0c01714
Cryst. Growth Des. 2021, 21, 2793−2806

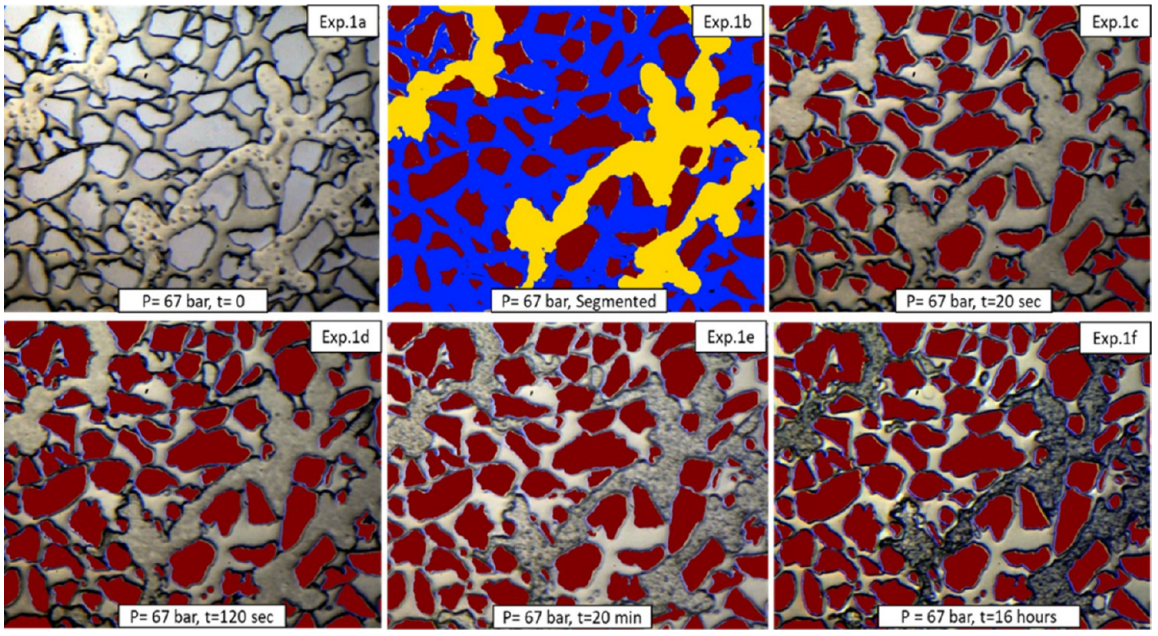

Figure 2. CO_2 hydrate formation from liquid CO_2 (yellow) and water (blue) at P = 67 bar and T = 3.5 °C (Exp. 1). (a,b) Initial fluid distribution. (c) CO_2 hydrate film encapsulates the liquid CO_2. (d) Rearrangement of the liquid interfaces during hydrate film growth. (e,f) The hydrate film surrounding the liquid CO_2 thickens with time.

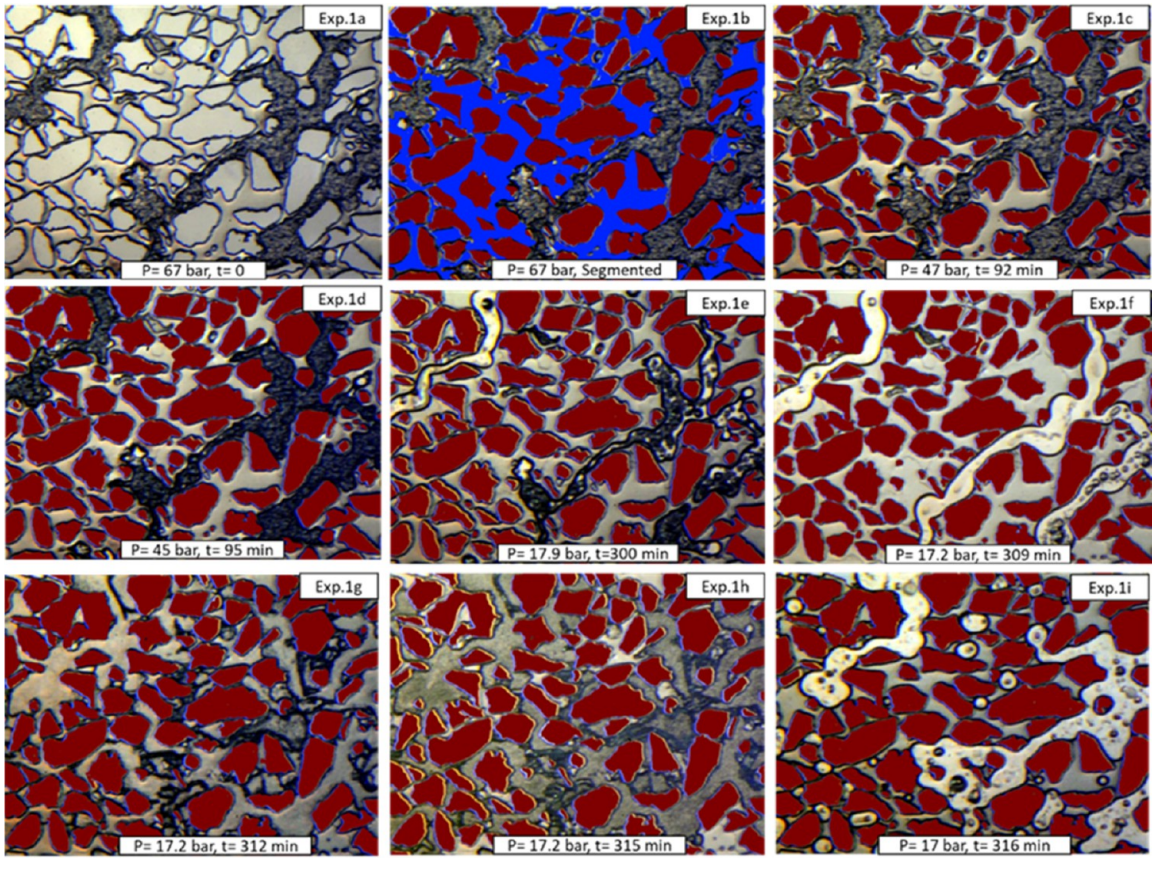

Figure 3. CO_2 hydrate dissociation by pressure depletion at a constant volumetric rate equal to 10 mL/h (Exp. 1). The system temperature is constant and equal to 3.5 °C. (a,b) Initial fluid and CO_2 hydrate distribution. (c,d) Hydrate-encapsulated liquid CO_2 converts to gaseous CO_2 above the CO_2 hydrate equilibrium pressure. (e,f) The CO_2 hydrate film dissociates as the pressure is lowered below the CO_2 hydrate equilibrium pressure. (g,h) Rapid reformation of CO_2 hydrates occurs. (i) Complete CO_2 hydrate dissociation.

The pressure was also sufficiently high to allow for three phases to coexist prior to hydrate formation: water, CH_4-rich gas, and CO_2-rich liquid. Whether three separate phases existed or not depended on the amount of CH_4 relative to the

https://doi.org/10.1021/acs.cgd.0c01714
Cryst. Growth Des. 2021, 21, 2793−2806

Table 2. List of Pressure and Temperature Conditions during Hydrate Formation at Different Initial Fluid Saturations[a]

	constant P and T		initial saturation		
Exp.	P (bar)	T (°C)	S_g	S_l	S_w
2	64	3.5	0.62	0	0.38
3	45	2.2	0.55	0	0.45
4	65	1.7	0.05	0.30	0.65
5	65	3.1	0.34	0	0.66
6	65	3.5	0.04	0.01	0.95

[a] S_g denotes CH_4-rich gas saturation and S_l denotes CO_2-rich liquid saturation.

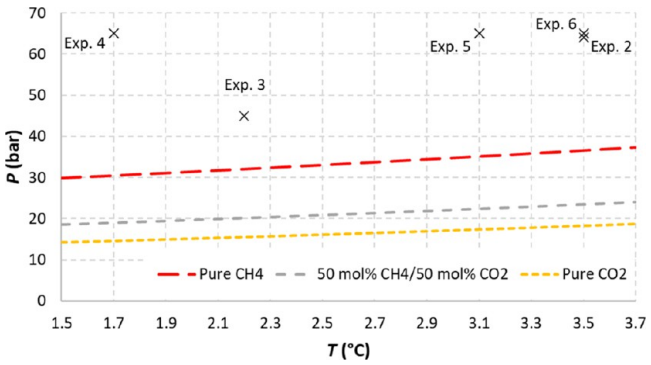

Figure 4. Hydrate-forming conditions (constant P and T) for all experiments. The equilibria pressures are calculated by the software PVTsim Nova.

amount of CO_2 that was present in the pore space.[31] A mixture of CH_4 and CO_2 that allowed for the coexistence of three phases was achieved in Exp. 4 and 6.

3.2.1.1. Low Initial Water Saturation. Two experiments (Exp. 2 and 3) had a low initial water saturation with the remainder of the pore space saturated with CH_4-rich gas containing dissolved CO_2. The temperature and pressure were 64 bar and 3.5 °C, respectively, during hydrate growth in Exp. 2 and the formation sequence is detailed in Figure 5. The hydrate growth started at the gas−water interface and encapsulated the gas phase within seconds (Figure 5c). The water remained as liquid during the first 6 min of the formation (Figure 5d), but eventually the liquid water crystallized into solid hydrates (Figure 5e). The crystallization of the water phase transpired gradually and simultaneously in the entire FOV. The final fluid configuration consisted of a mixture of massive hydrates and hydrate-encapsulated gas (Figure 5f). The thickness of the hydrate film that encapsulated the gas phase varied from pore to pore based on the local availability of gas and water. The liquid water was fully consumed since water was the limiting component of the hydrate growth process.

The hydrate formation pattern was similar in Exp. 3 where the pressure and temperature were 45 bar and 2.2 °C, respectively (Figure 6). However, in this experiment, a couple of isolated gas bubbles existed in the pore space prior to hydrate formation in addition to the continuous gas phase (Figure 6a,b). These gas bubbles were not affected by the initial hydrate film that swept the entire gas−water interface of the continuous gas phase (Figure 6c). This shows that the initial hydrate nucleation originated at discrete places. Once the hydrate nucleated at a point on the gas−water interface, the hydrate film spread quickly to cover the entire gas−water interfacial area. At the same time, neighboring gas bubbles were unaffected by this hydrate formation for several minutes. Instead, the isolated gas bubbles started to dissolve into the liquid water to sustain hydrate formation in the water phase (Figure 6d). The liquid water gradually crystallized into hydrates (Figure 6e) and the final fluid configuration (Figure 6f) mimicked the final configuration obtained in Exp. 2.

3.2.1.2. High Initial Water Saturation. The pore space was saturated with sufficient CO_2 to allow for a separate CO_2-rich liquid phase to exist in Exp. 4. The remainder of the pore space was filled with water and a couple of CH_4-rich gas bubbles (Figure 7). The gas bubbles were floating on top of the CO_2-rich liquid phase because of the buoyancy (Figure 7a,b). The thermodynamic driving force was strong as the

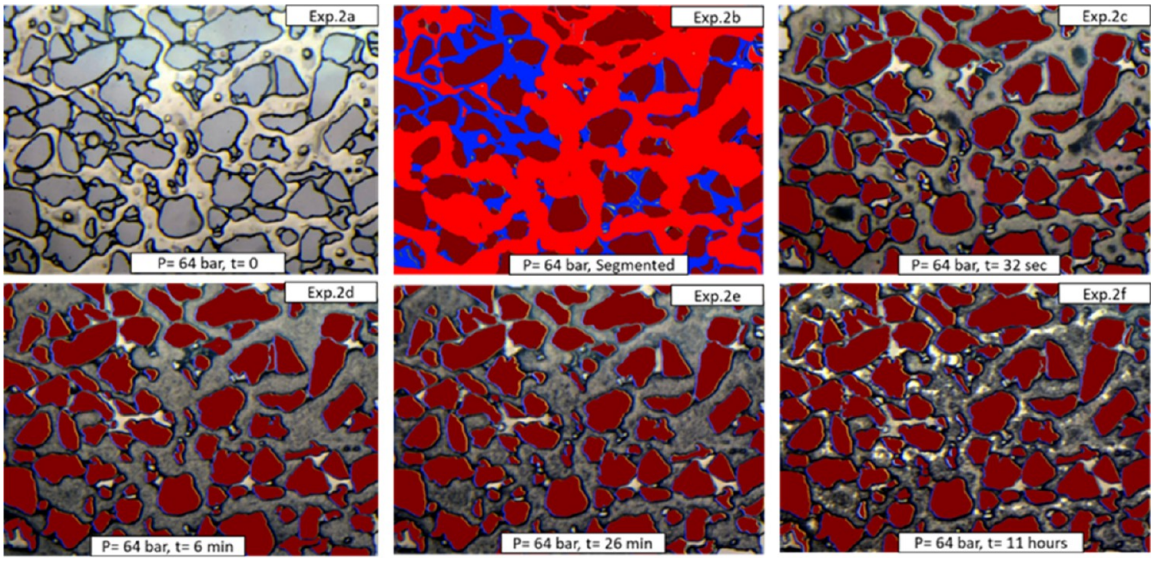

Figure 5. Hydrate formation from CH_4-rich gas (red) and liquid water (blue) at P = 64 bar and T = 3.5 °C (Exp. 2). (a,b) Initial fluid distribution. (c) Hydrate film encapsulates the gas phase. (d) Liquid water starts to crystallize into hydrates. (e,f) The hydrate film grows thicker in some regions of the pore space at the expense of other regions where the hydrate film gets thinner.

https://doi.org/10.1021/acs.cgd.0c01714
Cryst. Growth Des. 2021, 21, 2793−2806

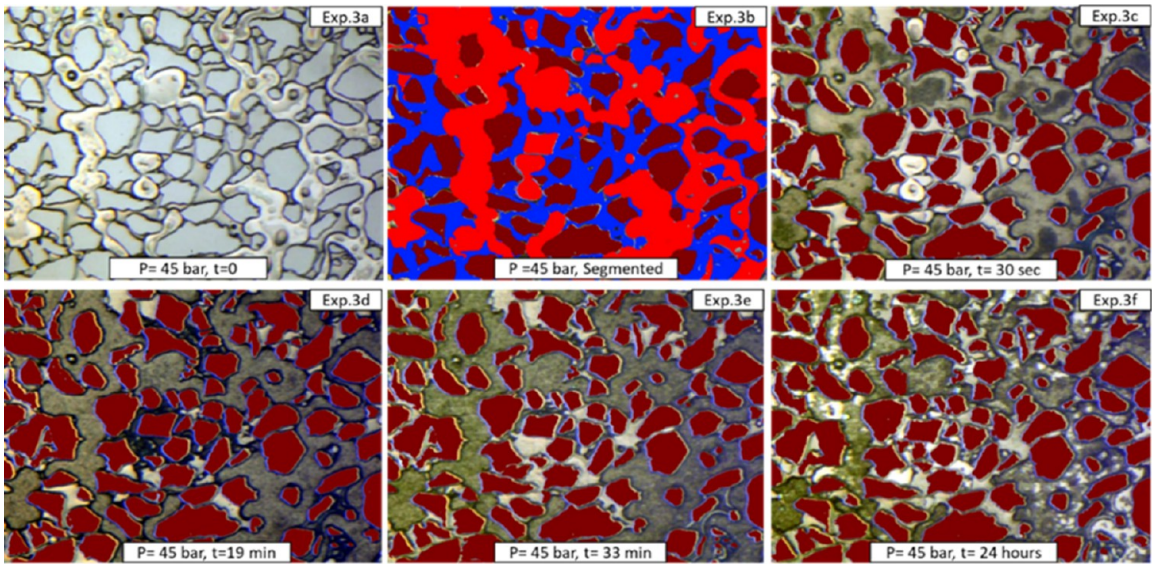

Figure 6. Hydrate formation from CH_4-rich gas (red) and liquid water (blue) at P = 45 bar and T = 2.2 °C (Exp. 3). (a,b) Initial fluid distribution. (c) The hydrate film encapsulates the gas phase except from the isolated gas bubbles. (d) The liquid water starts to crystallize into hydrates and the isolated gas bubbles dissolve into the water. (e,f) The hydrate film grows thicker in some regions of the pore space.

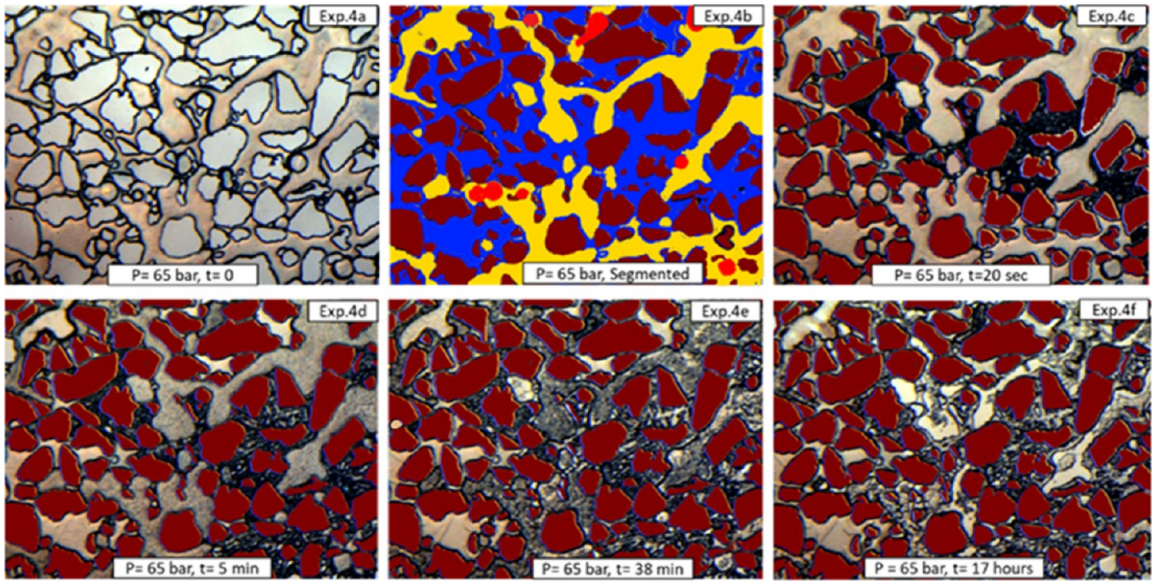

Figure 7. Hydrate formation from CH_4-rich gas (red), CO_2-rich liquid (yellow), and liquid water (blue) at P = 65 bar and T = 1.7 °C (Exp. 4). (a,b) Initial fluid distribution. (c) Liquid water starts to crystallize into solid hydrates. (d) CH_4-rich gas bubbles dissolve in the CO_2-rich liquid as the hydrate film grows on the CO_2-rich liquid–water interface. (e,f) The pore space is eventually saturated with CO_2-rich liquid completely immobilized by solid hydrates.

pressure and temperature were 65 bar and 1.7 °C, respectively. This resulted in a swift hydrate formation where the water phase started to crystallize after a few seconds before a hydrate film was visible on the CO_2-rich liquid–water interface (Figure 7c). The hydrate film appeared a couple of minutes later and the separate CH_4-rich gas bubbles dissolved in the CO_2-rich liquid as the hydrate film grew thicker (Figure 7d). Some of the water crystallized into faceted transparent hydrates (lower left corner Figure 7d–f), while other parts of the liquid water crystallized into a mixture of massive hydrates, hydrate films, and entrapped CO_2-rich liquid. Notice that despite the initial water saturation of 0.65 frac., the hydrate formation was still governed by an excess gas (liquid CO_2) supply and eventually all the water converted to hydrates. During this last stage of the hydrate formation process, taking several hours in the FOV, the hydrate distribution rearranged itself because of Ostwald ripening; large hydrate crystals continued to grow at the expense of small hydrate crystals. Some of the hydrate films that initially covered the CO_2-rich liquid phase dissociated to fuel further hydrate formation in other pores, leaving a substantial part of the pore space saturated with CO_2-rich liquid (Figure 7f). The CO_2-rich liquid was left completely immobilized by surrounding massive hydrates and with no supply of liquid water that could sustain the hydrate growth.

The initial fluid saturation was 0.66 frac. of water and 0.34 frac. of CH_4-rich gas with no separate CO_2-rich liquid phase in Exp. 5. The hydrate formation was conducted at a constant

https://doi.org/10.1021/acs.cgd.0c01714
Cryst. Growth Des. 2021, 21, 2793–2806

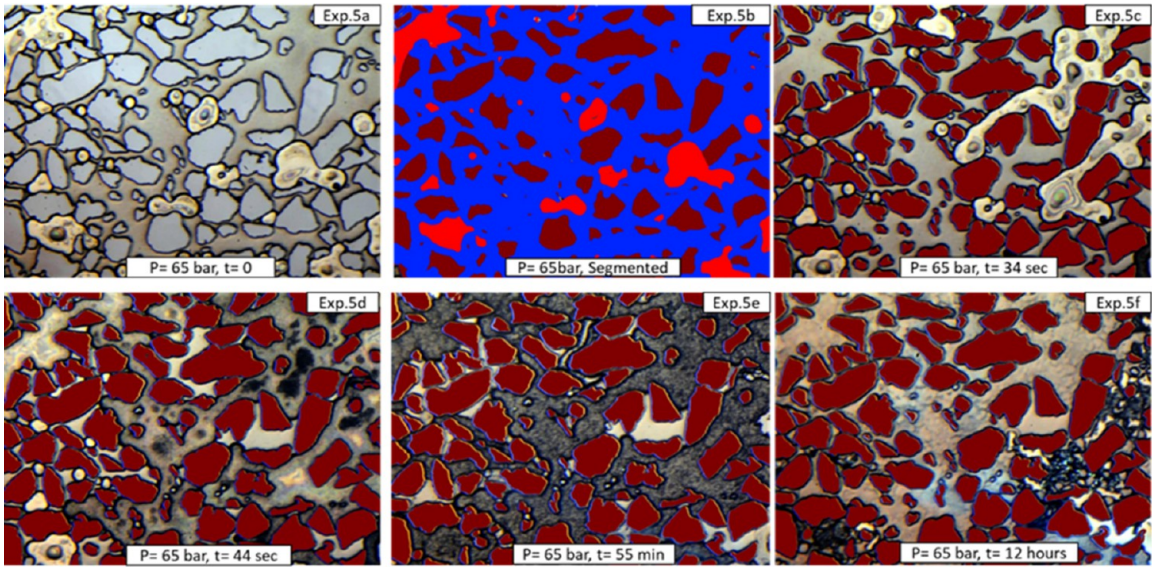

Figure 8. Hydrate formation from CH_4-rich gas (red) and liquid water (blue) at P = 65 bar and T = 3.1 °C (Exp. 5). (a,b) Initial fluid distribution. (c,d) A hydrate film spreads across the gas−water interfacial area of the continuous gas phase. (e,f) The hydrate film grows thicker with time until nearly all the gas is consumed.

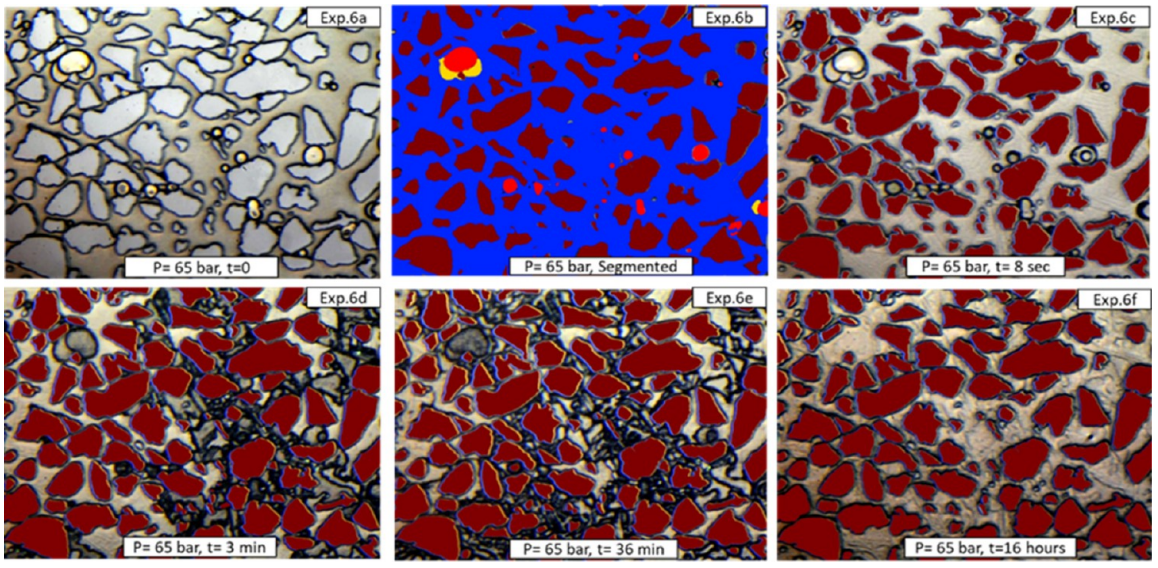

Figure 9. Hydrate formation from CH_4-rich gas (red), CO_2-rich liquid (yellow), and liquid water (blue) at P = 65 bar and T = 3.5 °C (Exp. 6). (a,b) Initial fluid distribution. (c) Liquid water crystallizes immediately to solid hydrates. (d) Part dissociation of the solid hydrates. (e,f) Hydrates reform and the pore space is eventually saturated with 100% hydrates.

pressure and temperature of 65 bar and 3.1 °C, respectively, and the growth process is detailed in Figure 8. The growth of hydrates initiated at the gas−water interface while the CH_4-rich gas was flowing through the FOV (Figure 8a−c). Notice how the hydrate layer was spreading across the gas−water interfacial area from image c to d in Figure 8 in a time period of 10 s. Again, the isolated gas bubbles that were not connected to the continuous gas phase were the last to develop hydrate films (Figure 8d). The hydrate film grew thicker with time (Figure 8e) and the local supply of liquid water in the FOV was sufficient to convert nearly all of the gas to solid hydrates. Most of the pore space was eventually saturated with massive hydrates and a few trapped unconverted gas pockets (Figure 8f).

Hydrates were formed from close to 100% water containing dissolved CH_4 and CO_2 in Exp. 6. A few CH_4-rich gas bubbles and CO_2-rich liquid droplets were also present prior to hydrate formation (Figure 9a,b). The hydrate-forming conditions were P = 65 bar and T = 3.5 °C. The initial hydrate growth occurred instantaneously and the entire water phase in the FOV crystallized to solid hydrates within seconds (Figure 9c). The encapsulation of the gas bubbles transpired rapidly and the CH_4-rich gas bubbles and CO_2-rich liquid droplets temporarily maintained their original shape (upper left corner of image d in Figure 9). However, a profound transformation of the hydrate morphology occurred from the initial instantaneous crystallization of the liquid water until long-term stability was achieved after 16 h. A couple of minutes after the water had crystallized to solid hydrates,

https://doi.org/10.1021/acs.cgd.0c01714
Cryst. Growth Des. 2021, 21, 2793−2806

fluids (gas or liquid) were expelled from the solid hydrate phase (Figure 9d). The initial crystallization was clearly not thermodynamically stable and a partial dissociation of the hydrates followed. Several factors may have caused this reconfiguration of the hydrate crystals, which all relate to the instantaneous hydrate formation: (1) the rapid initial hydrate nucleation may have caused significant local heating. Initial dissipation of the exothermic heat was slow due to poor heat convection caused by zero fluid mobility. The liberated fluids (gas or liquid) slowly started to form hydrates again (Figure 9e) as the local temperature was restored to the system temperature. (2) The water phase may have been undersaturated with CH_4 and CO_2 in other parts of the micromodel at the time hydrates formed rapidly in the FOV. Partial dissociation was then inflicted by hydrate formers dissolving into the water phase. (3) The rapid initial hydrate nucleation may have resulted in hydrate crystals with a low cage occupancy, which would have a destabilizing effect on the hydrate structure. Nonetheless, the pore space was ultimately saturated with 100% massive hydrates (Figure 9f). Similar observations of crystal coarsening due to Ostwald ripening are reported in the literature.[4,32]

3.2.2. Dissociation of Hydrates with Varying Compositions. A stepwise pressure reduction technique was implemented to unveil the range of dissociation pressure values in each experiment (Table 3). The dissociation sequence was bound by the equilibrium pressure for pure CH_4 hydrates and the equilibrium pressure for pure CO_2 hydrates at the given system temperature (Figure 10). The pressure range at which the hydrates dissociated was therefore indicative of the relative amounts of CH_4 and CO_2 present in the hydrate structure. The effect of hydrate dissociation kinetics was accounted for by allowing the hydrate phase transitions to occur for 30 min for each pressure value. However, this might not always be sufficient time for the phase transitions to occur in the entire pore space of the micromodel, depending on the hydrate morphology and distribution within the pores. The pressure values at which dissociation events were observed could therefore be affected by mass transport and fluid transmissibility, especially in the case when the pores were filled with pore-spanning massive hydrates.

Table 3. Overview of Initial and Final Dissociation Pressures for Each Experiment[a]

	constant temperature	equilibrium pressures		dissociation observed	dissociation completed
Exp.	T (°C)	P_{CH_4} (bar)	P_{CO_2} (bar)	P (bar)	P (bar)
2	3.5	36.6	18.3	32	19
3	2.2	32.1	15.6	29	20
4	1.7	30.5	14.7	31	16
5	3.1	35.1	17.4	33	27
6	3.3	35.8	17.8	20	17

[a]The equilibria pressures are calculated by the software PVTsim Nova.

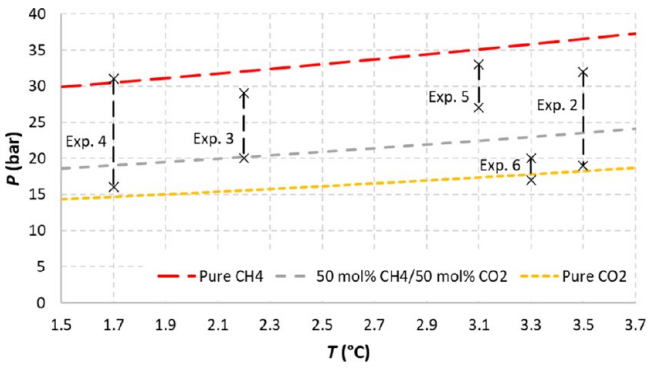

Figure 10. Plot of initial and final dissociation pressures for each experiment. The equilibria pressures are calculated by the software PVTsim Nova.

3.2.2.1. Hydrate Film Dissociation. The final hydrate distribution was dominated by hydrate films surrounding the gas phase in Exp. 2 and 3. The large fraction of gas in the pore space ensured that the pressure depletion was effectuated throughout the entire pore space and resulted in mixing of fluids and redistribution of fluid phases prior to initial hydrate dissociation. This was observed during pressure depletion in Exp. 2, where water invaded the lower part of the FOV (Figure 11b) as the pressure was lowered to 38 bar. As the pressure was lowered further to 37 bar, which was approximately equal to the equilibrium pressure of pure CH_4 hydrates, reformation of hydrates occurred in the entire FOV. The newly formed liquid water crystallized into solid hydrates while a thicker hydrate film developed around the gas phase (Figure 11c–e). The mobilization of fluids associated with the pressure depletion inflicted a substantially increase in the hydrate saturation within the FOV.

The first sign of hydrate dissociation was observed when the pressure was lowered to 32 bar (Figure 11f). The gas-encapsulating hydrate film dissociated first and left the liberated gas immobilized surrounded by solid massive hydrates (Figure 11f,g). At the same time as the hydrate film was dissociating, further hydrate reformation occurred at P = 25 bar as some of the newly liberated gas reacted with liquid water (Figure 11h–j). The mechanism for this simultaneous hydrate growth and decomposition is believed to originate from the different hydrate equilibrium pressures for CH_4 and CO_2. The hydrate with a certain composition of CH_4 and CO_2 dissociated at a distinct pressure. The liberated CH_4 gas could not react with water and reform to hydrates at that pressure, but the liberated CO_2 gas could, as the pressure was still above the equilibrium pressure of pure CO_2 hydrates. The effect of the stepwise pressure reduction was therefore to concentrate the amount of CO_2 located in the hydrate phase.[15] The process led to the highest hydrate saturation being achieved at P = 25 bar with most of the pore space saturated with massive hydrates and a trapped gas phase enriched with CH_4 (Figure 11j).

The next pressure step to P = 24 bar invoked dissociation of the newly formed hydrate but the dissociation process was slow because of the solid non-porous nature of the hydrate phase (Figure 11k–o). The dissociation front spread across the pore network as the hydrate in one pore had to dissociate before the dissociation front moved to the next pore. The liberated gas was effectively transported downstream by the connected gas phase. The entire hydrate phase was fully dissociated as the pressure was lowered to 19 bar, which was approximately equal to the equilibrium pressure of pure CO_2 hydrates.

3.2.2.2. Dissociation of Massive Hydrates. The pore space was predominantly saturated with massive non-porous

https://doi.org/10.1021/acs.cgd.0c01714
Cryst. Growth Des. 2021, 21, 2793–2806

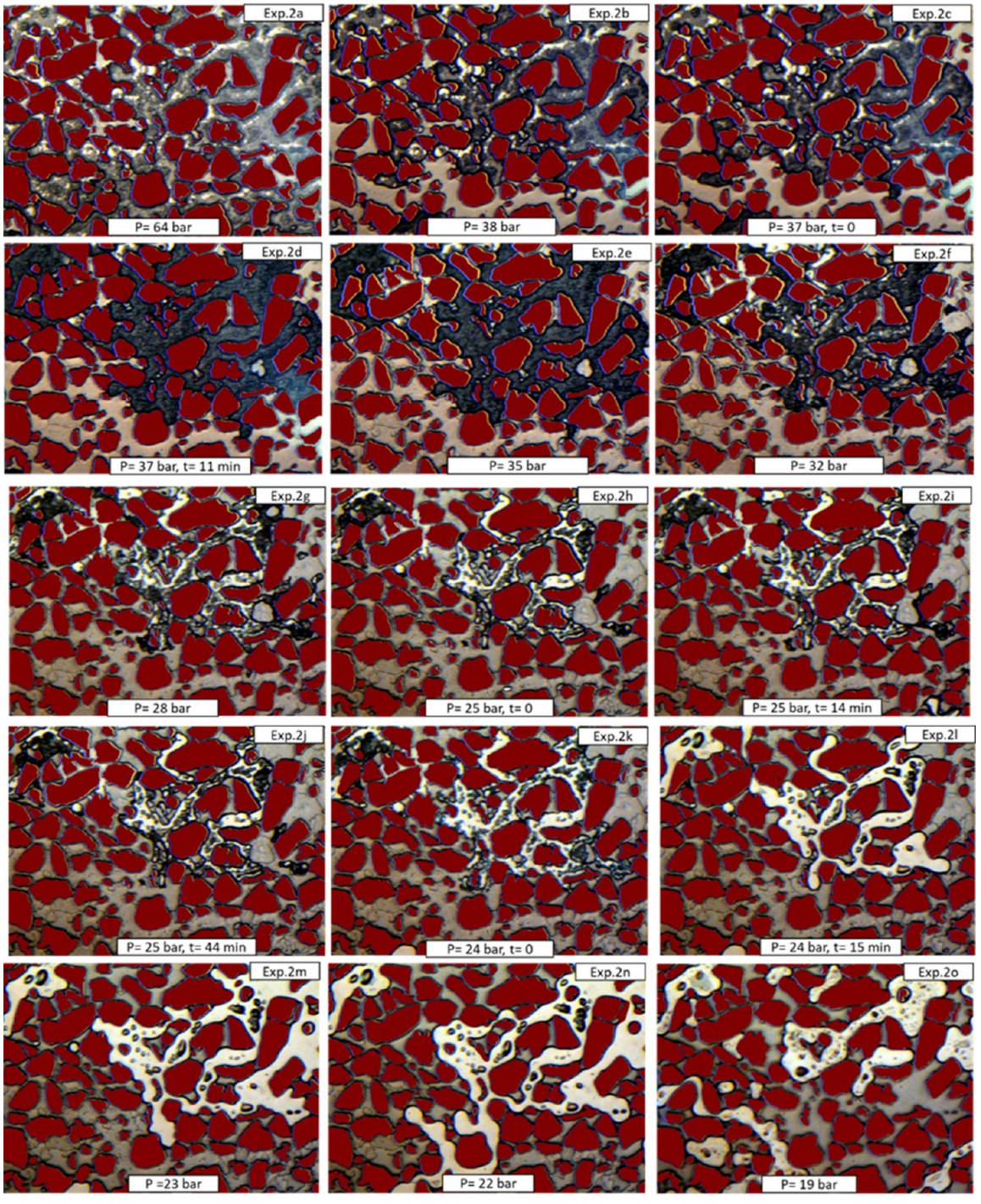

Figure 11. Hydrate dissociation by stepwise pressure depletion (Exp. 2). The system temperature is constant and equal to 3.5 °C. (a) Fluid and hydrate saturation before pressure depletion. (b) Water invades the lower part of the pore space during pressure depletion. (c−e) Hydrate reformation. (f) Initial dissociation of the hydrate film. (g−j) Simultaneous hydrate dissociation and reformation. (k−o) Slow dissociation until complete hydrate dissociation.

hydrates after hydrate formation in Exp. 4−6. This meant that the pressure depletion was necessarily not immediately transmitted throughout the pore network as the solid hydrate could block the pore channels prior to dissociation. The local pressure in the pores in the FOV could therefore deviate from the pressure recorded in the pump. The first sign of a phase transition was observed when the pump pressure was lowered to 31 bar in Exp. 4 (Figure 12), which was equal to the equilibrium pressure for pure CH_4 hydrates. A small bubble of gas appeared (highlighted in image b in Figure 12) in a pore saturated by an immobile CO_2-rich liquid surrounded by hydrates. The bubble originated either from local hydrate dissociation or from CH_4 gas coming out of the solution from the CO_2-rich liquid. The gas bubble can be seen floating on top of the CO_2-rich liquid and the hydrate film in Figure 12c. Another gas bubble appeared as the pressure was lowered to 27 bar (highlighted in image d in Figure 12). The bubble appeared in a pore that was saturated with a massive non-

https://doi.org/10.1021/acs.cgd.0c01714
Cryst. Growth Des. 2021, 21, 2793−2806

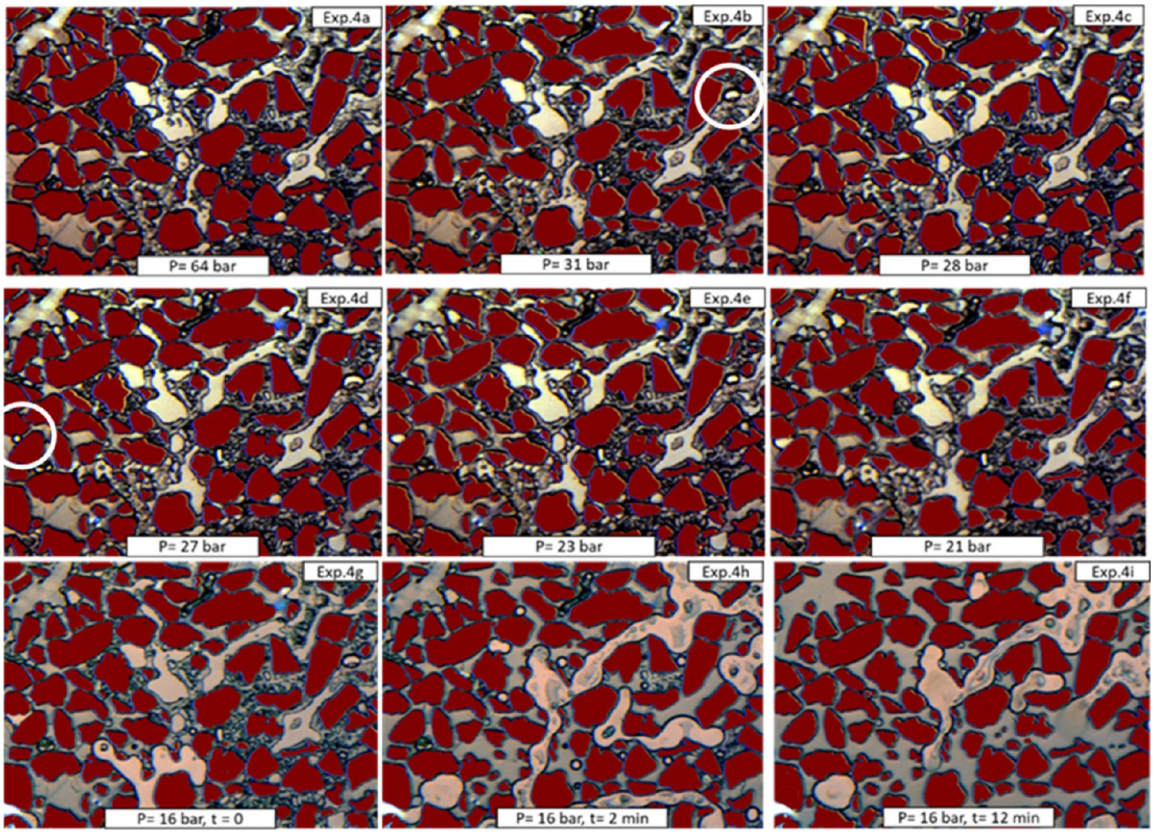

Figure 12. Hydrate dissociation by stepwise pressure depletion (Exp. 4). The system temperature is constant and equal to 1.7 °C. (a) Fluid and hydrate saturation before pressure depletion. (b) A small gas bubble appears (white circle). (c) The gas bubble increases slowly as the pressure is depleted. (d) Another gas bubble appears in a pore saturated by massive hydrates (white circle). (e,f) The gas bubbles increase slightly as the pressure is depleted. (g–i) All hydrates dissociate quickly as the pressure is lowered to 16 bar.

porous hydrate and was likely a sign of hydrate dissociation. Anyhow, the two gas bubbles remained immobile and increased slowly in size as the pressure was depleted to 16 bar. At that time, a rapid hydrate dissociation occurred in the entire FOV (Figure 12g–i). The pressure depletion finally reached the FOV and the dissociation transpired quickly when the trapped immobile gas phase could flow downstream. The dissociation characteristics seen in this experiment show that the pore pressure may be highly variable during pressure depletion, which can lead to local small-scale phase transitions without affecting the overall integrity and distribution of the hydrate and fluid phases.

The FOV was mainly saturated with massive non-porous hydrates in Exp. 5 with some pores saturated with hydrate films and immobile CH_4-rich gas (Figure 13). The equilibrium pressure for pure CH_4 hydrates was 35 bar (PVTsim Nova) and initial hydrate dissociation was observed when the pressure was lowered to 33 bar (highlighted in Figure 13b). The hydrate dissociation started in a pore saturated with a hydrate film that encapsulated the gas in the pore. No further dissociation occurred as the pressure was lowered to 30 bar (Figure 13c). The pressure was now kept constant to 30 bar for 14 h due to running the experiment overnight. Nearly all the hydrates dissociated during this time; both the massive non-porous hydrate and the hydrate films covering the gas phase. However, hydrates remained in three separate locations in the FOV; all the locations were characterized by small and narrow pores (Figure 13d). The dissociation continued slowly as the pressure was lowered to 28 bar, but still some hydrate crystals were observed in one of the pores (Figure 13f). A rapid reformation of hydrates occurred shortly after the pressure was set to 28 bar (Figure 13f,g). The largest connected gas phase in the FOV was instantly covered by a hydrate film, while other smaller gas bubbles did not form hydrates (Figure 13g). The selectiveness of the hydrate reformation was probably due to different contents of CO_2 in the different distinctive gas phases. The phase transitions were chaotic during this period and simultaneous hydrate growth and dissociation were observed. After 18 min transpired, most of the hydrates dissociated again and only patchy disconnected hydrates were spread across the entire FOV (Figure 13k). No further phase transitions occurred during the next 42 min and the pressure was lowered to 27 bar at which the remaining hydrates gradually dissociated, leaving the gas phase covered with water droplets (Figure 13l).

Hydrate dissociation initiated when the pressure was lowered to 20 bar in Exp. 6. The equilibrium pressure for pure CH_4 hydrates was 36 bar (PVTsim Nova) and the stepwise pressure reduction was therefore started at P = 37 bar, meaning that the pressure depletion had lasted for almost 9 h before hydrate dissociation began in the FOV. The pore space was completely saturated with massive non-porous hydrates (Figure 14) and inhibited the pressure depletion to propagate through the pore network. At P = 20 bar, the dissociation front reached the FOV and approximately 50% of the hydrates dissociated after 30 min (Figure 14b–d). The dissociation front moved from pore to pore and the liberated gas flowed downstream. Later, as the pressure depletion

https://doi.org/10.1021/acs.cgd.0c01714
Cryst. Growth Des. 2021, 21, 2793–2806

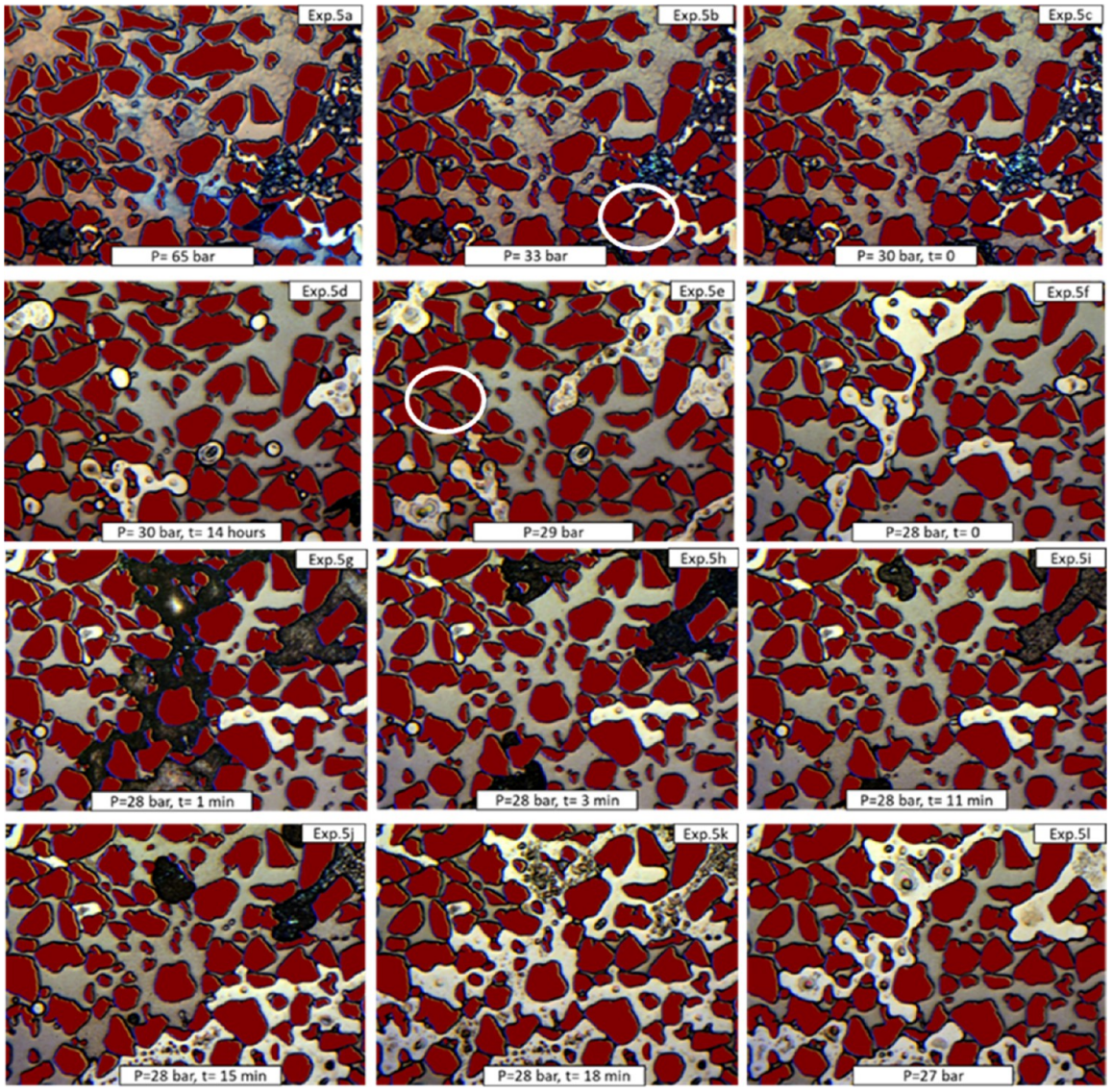

Figure 13. Hydrate dissociation by stepwise pressure depletion (Exp. 5). The system temperature is constant and equal to 3.1 °C. (a) Fluid and hydrate saturation before pressure depletion. (b) Start of hydrate dissociation (white circle). (c,d) Nearly all hydrates dissociate during 14 h at P = 30 bar. (e) Hydrate dissociation continues, but still some hydrates are left (white circle). (f,g) Rapid reformation of hydrates across the connected gas phase at P = 28 bar. (h–k) Both hydrate reformation and dissociation at P = 28 bar. (l) Complete hydrate dissociation as the pressure is lowered to 27 bar. Notice the water droplets that are covering the gas phase.

continued, the liberated gas started to segregate into two phases (Figure 14e–j). One portion of the liberated gas became coated with a reformed hydrate layer, while the rest of the gas flowed freely without forming hydrates. This was interpreted as a separation of the mixture of CH_4 and CO_2 gas that was liberated from the initial dissociation into a CO_2-rich gas that reformed hydrates and a CH_4-rich gas that could not form hydrates. The CH_4-rich gas floated on top of the hydrate-coated CO_2-rich gas. The produced gas mixture was consequently enriched with CH_4 compared to the original mixture of CH_4 and CO_2 as some of the CO_2 was retained in the pores by the reformed hydrate layer. The reformed hydrate layer persisted until the pressure was reduced to 17 bar (Figure 14k–l), which is close to the theoretical dissociation pressure for pure CO_2 hydrates.

The observations made in this study demonstrate the possibility of producing gas liberated from local hydrate dissociation while simultaneously reforming hydrates in other parts of the sediments. This is relevant for the proposed production method where CO_2 injection in CH_4 hydrate reservoirs is followed by pressure depletion to enhance the CH_4 gas recovery. The effect of CO_2 injection alone depends heavily on the transmissibility of the reservoir through the hydrate and water saturation. The injected CO_2 must be able to penetrate deep into the reservoir to maximize the interfacial area between the CO_2 and the CH_4 hydrates. However, maintaining a good volumetric sweep is challenging since most candidate reservoirs for CH_4 gas production contain high hydrate saturations (S_H > 60%) and excess water.[33] The CO_2 injectivity is highly sensitive to CH_4 hydrate blockage of the pore space as well as formation of CO_2 hydrates with the excess pore water. The role of pressure depletion is therefore critical for improving the injectivity of CO_2. Partial dissociation of CH_4 hydrates by pressure depletion liberates CH_4 gas and water and consequently enhances the fluid permeability. This allows for CO_2 to displace CH_4 gas and

https://doi.org/10.1021/acs.cgd.0c01714
Cryst. Growth Des. 2021, 21, 2793–2806

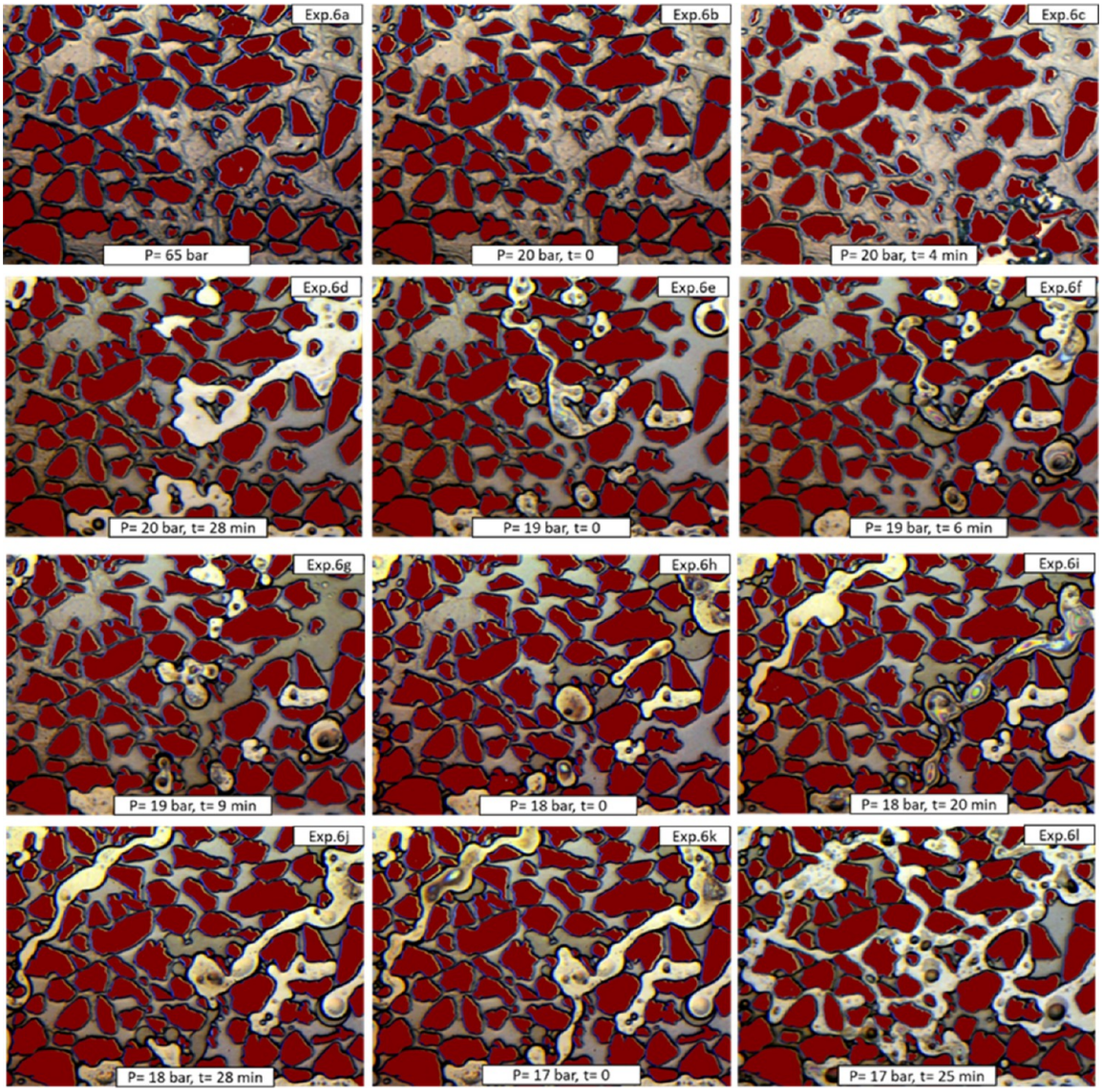

Figure 14. Hydrate dissociation by stepwise pressure depletion (Exp. 6). The system temperature is constant and equal to 3.3 °C. (a) The pore space is completely saturated with massive non-porous hydrates prior to pressure depletion. (b–d) Approximately 50% of the hydrates dissociate at P = 20 bar. (e–j) Liberated gas from the hydrate dissociation segregates into two gas phases: one gas phase is floating on top of the other gas phase, which is covered and immobilized by a hydrate film. (k–l) The hydrate film dissociates completely as the pressure is lowered to 17 bar.

propagate deeper into the formation until the CO_2 eventually reacts and forms hydrates with the pore water. The results presented in this study (highlighted by Exp. 6) show that CH_4-rich gas can flow in pores simultaneously as CO_2-rich gas is being trapped by the formation of hydrate films. Injecting CO_2 from one well while producing CH_4 gas by pressure depletion in another well has thus the potential to increase the CH_4 gas recovery toward the recovery values expected by full-scale pressure depletion. The added benefit provided by the CO_2 injection is substantial carbon storage through CO_2 hydrate formation, which also contributes to maintaining the geomechanical stability of the formation. The target reservoir pressure for the combined injection and production would be between the equilibrium pressure of CH_4 hydrates and CO_2 hydrates in reservoirs with temperatures below ∼10 °C. A production technique involving the injection of 23% CO_2 and 77% nitrogen has already successfully been tested through the single-well field pilot conducted on the North Slope of Alaska.[34] Alternatively, a produce first (CH_4) and inject later (CO_2) approach could be implemented to avoid the cost of CH_4 and CO_2 separation at the production facility.[35]

4. CONCLUSIONS

A high-pressure micromodel was used to visualize phase transitions of CH_4/CO_2 hydrates in sandstone pores. Hydrates with varying compositions of CH_4 and CO_2 were formed at constant P and T from different initial fluid saturations and gradual dissociation was conducted by stepwise depressurization. The pore-scale visualization of the phase transitions revealed the following:

- The hydrate formation pattern varied considerably between experiments and depended on a combination of initial CO_2 content relative to the CH_4 content, initial water saturation, initial fluid distribution, and thermodynamic driving forces. Initial hydrate formation was observed both on the gas–water interface (hydrate film) and in the liquid water phase (massive hydrates).

https://doi.org/10.1021/acs.cgd.0c01714
Cryst. Growth Des. 2021, 21, 2793–2806

- The hydrate film spread quickly (within seconds) to cover the entire gas−water interface once hydrate nucleation started. However, isolated gas bubbles that were disconnected from the continuous gas phase developed hydrate films later and independent of the hydrate film on the continuous gas phase.
- Stepwise pressure depletion of hydrates caused simultaneous hydrate dissociation and hydrate reformation as the pressure was lowered below the equilibrium pressure of pure CH_4 hydrates and above the equilibrium pressure of pure CO_2 hydrates. The overall hydrate saturation increased and the hydrate distribution became more homogenous as hydrates reformed during gas production.

AUTHOR INFORMATION

Corresponding Author

Stian Almenningen − *Department of Physics and Technology, University of Bergen, Bergen 5007, Norway;* orcid.org/0000-0002-2839-8503; Email: stian.almenningen@uib.no

Authors

Jyoti Shanker Pandey − *Center for Energy Resource Engineering (CERE), Department of Chemical Engineering, Technical University of Denmark, Lyngby 2800, Denmark;* orcid.org/0000-0002-3714-4513

Ørjan Strand − *Department of Physics and Technology, University of Bergen, Bergen 5007, Norway*

Nicolas von Solms − *Center for Energy Resource Engineering (CERE), Department of Chemical Engineering, Technical University of Denmark, Lyngby 2800, Denmark*

Geir Ersland − *Department of Physics and Technology, University of Bergen, Bergen 5007, Norway*

Complete contact information is available at: https://pubs.acs.org/10.1021/acs.cgd.0c01714

Notes

The authors declare no competing financial interest.

REFERENCES

(1) Ersland, G.; Husebø, J.; Graue, A.; Baldwin, B. A.; Howard, J.; Stevens, J. Measuring gas hydrate formation and exchange with CO2 in Bentheim sandstone using MRI tomography. *Chem. Eng. J.* **2010**, *158*, 25−31.

(2) Falenty, A.; Qin, J.; Salamatin, A. N.; Yang, L.; Kuhs, W. F. Fluid Composition and Kinetics of the in Situ Replacement in CH4-CO2Hydrate System. *J. Phys. Chem. C* **2016**, *120*, 27159−27172.

(3) Zhao, J.; Zhang, L.; Chen, X.; Fu, Z.; Liu, Y.; Song, Y. Experimental Study of Conditions for Methane Hydrate Productivity by the CO2 Swap Method. *Energy Fuels* **2015**, *29*, 6887−6895.

(4) Pan, M.; Ismail, N. A.; Luzi-Helbing, M.; Koh, C. A.; Schicks, J. M. New Insights on a μm-Scale into the Transformation Process of CH4 Hydrates to CO2-Rich Mixed Hydrates. *Energies* **2020**, *13*, 5908.

(5) Tohidi, B.; Anderson, R.; Clennell, M. B.; Burgass, R. W.; Biderkab, A. B. Visual observation of gas-hydrate formation and dissociation in synthetic porous media by means of glass micromodels. *Geology* **2001**, *29*, 867−870.

(6) Katsuki, D.; Ohmura, R.; Ebinuma, T.; Narita, H. Visual observation of dissociation of methane hydrate crystals in a glass micro model: Production and transfer of methane. *J. Appl. Phys.* **2008**, *104*, 083514.

(7) Hauge, L. P.; Gauteplass, J.; Høyland, M. D.; Ersland, G.; Kovscek, A.; Fernø, M. A. Pore-level hydrate formation mechanisms using realistic rock structures in high-pressure silicon micromodels. *Int. J. Greenhouse Gas Control* **2016**, *53*, 178−186.

(8) Almenningen, S.; Flatlandsmo, J.; Kovscek, A. R.; Ersland, G.; Fernø, M. A. Determination of pore-scale hydrate phase equilibria in sediments using lab-on-a-chip technology. *Lab Chip* **2017**, *17*, 4070−4076.

(9) Almenningen, S.; Iden, E.; Fernø, M. A.; Ersland, G. Salinity Effects on Pore-Scale Methane Gas Hydrate Dissociation. *J. Geophys. Res.: Solid Earth* **2018**, *123*, 5599−5608.

(10) Almenningen, S.; Gauteplass, J.; Fotland, P.; Aastveit, G. L.; Barth, T.; Ersland, G. Visualization of hydrate formation during CO2 storage in water-saturated sandstone. *Int. J. Greenhouse Gas Control* **2018**, *79*, 272−278.

(11) Gauteplass, J.; Almenningen, S.; Ersland, G.; Barth, T.; Yang, J.; Chapoy, A. Multiscale investigation of CO2 hydrate self-sealing potential for carbon geo-sequestration. *Chem. Eng. J.* **2020**, *381*, 122646.

(12) Seo, Y.-T.; Lee, H. Multiple-Phase Hydrate Equilibria of the Ternary Carbon Dioxide, Methane, and Water Mixtures. *J. Phys. Chem. B* **2001**, *105*, 10084−10090.

(13) Zheng, R.; Fan, Z.; Li, X.; Negahban, S. Phase behavior of high-pressure CH4-CO2 hydrates in NaCl solutions. *Fuel* **2020**, *280*, 118549.

(14) Uchida, T.; Ikeda, I. Y.; Takeya, S.; Kamata, Y.; Ohmura, R.; Nagao, J.; Zatsepina, O. Y.; Buffett, B. A. Kinetics and Stability of CH4-CO2 Mixed Gas Hydrates during Formation and Long-Term Storage. *ChemPhysChem* **2005**, *6*, 646−654.

(15) Kwon, T.-H.; Kneafsey, T. J.; Rees, E. V. L. Thermal Dissociation Behavior and Dissociation Enthalpies of Methane-Carbon Dioxide Mixed Hydrates. *J. Phys. Chem. B* **2011**, *115*, 8169−8175.

(16) Sun, Y.-H.; Zhang, G.-B.; Carroll, J. J.; Li, S.-L.; Jiang, S.-H.; Guo, W. Experimental investigation into gas recovery from CH4-C2H6-C3H8 hydrates by CO2 replacement. *Appl. Energy* **2018**, *229*, 625−636.

(17) Buchgraber, M.; Castanier, L. M.; Kovscek, A. R. Microvisual Investigation of Foam Flow in Ideal Fractures: Role of Fracture Aperture and Surface Roughness. *SPE Annual Technical Conference and Exhibition*, San Antonio, Texas, USA, October 8−10, 2012.

(18) Almenningen, S.; Flatlandsmo, J.; Fernø, M. A.; Ersland, G. Multiscale Laboratory Verification of Depressurization for Production of Sedimentary Methane Hydrates. *SPE J.* **2017**, *22*, 138−147.

(19) Bylov, M.; Rasmussen, P. Experimental determination of refractive index of gas hydrates. *Chem. Eng. Sci.* **1997**, *52*, 3295−3301.

(20) Guo, J.; André, P.; Adam, M.; Panyukov, S.; Rubinstein, M.; DeSimone, J. M. Solution Properties of a Fluorinated Alkyl Methacrylate Polymer in Carbon Dioxide. *Macromolecules* **2006**, *39*, 3427−3434.

(21) Uchida, T.; Ebinuma, T.; Kawabata, J.; Narita, H. Microscopic observations of formation processes of clathrate-hydrate films at an interface between water and carbon dioxide. *J. Cryst. Growth* **1999**, *204*, 348−356.

(22) Almenningen, S.; Flatlandsmo, J.; Fernø, M. A.; Ersland, G. Direct Pore-Level Visualization of Methane Hydrate Growth in an Authentic Sandstone Replicate. *The 9th International Conference on Gas Hydrates*, Denver, Colorado, USA, June 25−30, 2017.

(23) Katsuki, D.; Ohmura, R.; Ebinuma, T.; Narita, H. Formation, growth and ageing of clathrate hydrate crystals in a porous medium. *Philos. Mag.* **2006**, *86*, 1753−1761.

(24) Tanaka, R.; Sakemoto, R.; Ohmura, R. Crystal growth of clathrate hydrates formed at the interface of liquid water and gaseous methane, ethane, or propane: variations in crystal morphology. *Cryst. Growth Des.* **2009**, *9*, 2529−2536.

(25) Saito, K.; Kishimoto, M.; Tanaka, R.; Ohmura, R. Crystal growth of clathrate hydrate at the interface between hydrocarbon gas mixture and liquid water. *Cryst. Growth Des.* **2011**, *11*, 295−301.

(26) Oya, S.; Aifaa, M.; Ohmura, R. Formation, growth and sintering of CO2 hydrate crystals in liquid water with continuous

CO2 supply: Implication for subsurface CO2 sequestration. *Int. J. Greenhouse Gas Control* **2017**, *63*, 386−391.
(27) Ueno, H.; Akiba, H.; Akatsu, S.; Ohmura, R. Crystal growth of clathrate hydrates formed with methane + carbon dioxide mixed gas at the gas/liquid interface and in liquid water. *New J. Chem.* **2015**, *39*, 8254−8262.
(28) He, Y.; Rudolph, E. S. J.; Zitha, P. L. J.; Golombok, M. Kinetics of CO2 and methane hydrate formation: An experimental analysis in the bulk phase. *Fuel* **2011**, *90*, 272−279.
(29) NIST Chemistry WebBook, SRD 69. *Thermophysical Properties of Fluid Systems*, 2018.
(30) Kou, X.; Li, X.-S.; Wang, Y.; Zhang, Y.; Chen, Z.-Y. Distribution and reformation characteristics of gas hydrate during hydrate dissociation by thermal stimulation and depressurization methods. *Appl. Energy* **2020**, *277*, 115575.
(31) Legoix, L.; Ruffine, L.; Donval, J.-P.; Haeckel, M. Phase Equilibria of the CH4-CO2 Binary and the CH4-CO2-H2O Ternary Mixtures in the Presence of a CO2-Rich Liquid Phase. *Energies* **2017**, *10*, 2034.
(32) Chen, X.; Espinoza, D. N. Ostwald ripening changes the pore habit and spatial variability of clathrate hydrate. *Fuel* **2018**, *214*, 614−622.
(33) Boswell, R.; Collett, T. S. Current perspectives on gas hydrate resources. *Energy Environ. Sci.* **2011**, *4*, 1206−1215.
(34) Boswell, R.; Schoderbek, D.; Collett, T. S.; Ohtsuki, S.; White, M.; Anderson, B. J. The Iġnik Sikumi Field Experiment, Alaska North Slope: Design, Operations, and Implications for CO2-CH4 Exchange in Gas Hydrate Reservoirs. *Energy Fuels* **2017**, *31*, 140−153.
(35) Englezos, P. Extraction of methane hydrate energy by carbon dioxide injection-key challenges and a paradigm shift. *Chin. J. Chem. Eng.* **2019**, *27*, 2044−2048.

https://doi.org/10.1021/acs.cgd.0c01714
Cryst. Growth Des. 2021, 21, 2793−2806